eprints@whiterose.ac.uk
https://eprints.whiterose.ac.uk/

Journal of Nuclear Engineering and Radiation Science

A Numerical Study of Turbulent Upward Flow of Super Critical Water in a 2×2 Rod Bundle with Non-uniform Heating

Bo Liu[1]
Department of Mechanical Engineering, the University of Sheffield
S32, 3 Solly Street, Sheffield, S1 4DE, UK
bo.liu@sheffield.ac.uk

Shuisheng He
Department of Mechanical Engineering, the University of Sheffield
S32, 3 Solly Street, Sheffield, S1 4DE, UK
s.he@sheffield.ac.uk

Charles Moulinec
Science and Technology Facilities Council
Daresbury Laboratory, Warrington, WA4 4AD, UK
charles.moulinec@stfc.ac.uk

Juan Uribe
EDF Energy R&D UK Centre
C22, George Begg Building, the University of Manchester, Manchester, M13 9PL, UK
juan.uribe@edfenergy.com

ABSTRACT

This work is part of a benchmarking exercise organized by an IAEA CRP in SuperCritical Water-cooled

Reactor (SCWR) thermal-hydraulics aimed at improving the understanding and prediction accuracy of the

thermal-hydraulic phenomena relevant to SCWRs. An experiment carried out using a 2×2 SCWR bundle at

University of Wisconsin-Madison was modelled using an open-source Computational Fluid Dynamics (CFD)

code - Code_Saturne. The k-ω Shear Stress Transport (SST) model was employed to account for the

buoyancy-aided turbulent flow in the fuel channel. Significant Heat Transfer Deterioration (HTD) was

---

[1] Corresponding author.

Journal of Nuclear Engineering and Radiation Science

observed in the boundary layer, which is commonly expected to occur in buoyancy-aided flows. For

comparison, simulations were also conducted using ANSYS Fluent with similar model setups.

1. INTRODUCTION

In order to obtain a cleaner, safer and more efficient future nuclear energy

source, the International Generation IV Forum was launched and six designs of nuclear

reactor systems have been selected for consideration, amongst which the SuperCritical

Water-cooled Reactor (SCWR) is the only water-cooled reactor. Such reactors have the

advantages of high thermal efficiency, compact system structure and low capital cost [1,

2]. As opposed to sub-critical conditions, heat transfer behavior of supercritical fluid

shows some surprising characteristics due to drastic changes in thermal-physical

properties, such as density, specific heat, dynamic viscosity and thermal conductivity in

the vicinity of the pseudo-critical temperature [3, 4]. Flows in such conditions are very

sensitive to the thermal and structural environment and tend to show sudden changes,

which poses great challenges to the prediction of this process and thus the design of the

SCWR.

One of the most significant concerns in using a supercritical fluid as a reactor

primary circuit coolant is 'Heat Transfer Deterioration' (HTD). This effect is caused by the

large variation in physical properties of a fluid (e.g. density and thermal conductivity)

near the pseudo-critical line [5]. A reduction in heat transfer can cause undesirably high

solid wall temperatures that put constraints on the material the reactor and/or fuel is

made of. Experimental studies on heat transfer of supercritical pressure fluids are still

limited due to the technical difficulty and high cost of equipment. However, the rapid

2

development of numerical techniques and the increase of computing capacity now allows the simulation of flows under supercritical conditions. In the past decades, state-of-the-art Computational Fluid Dynamics (CFD) has been used by many researchers to study flow and heat transfer of supercritical fluids in simple geometries, including circular pipes [6-12], plane channels [13-14] and annular channels [15-16], which have greatly enhanced the understanding of this phenomenon. However, these studies could not reach a consensus on the choice of a suitable turbulence model for supercritical flow simulations, as it has been found that the quality of the results produced by the various turbulence models used in these works changes significantly from case to case, as they are flow and geometry dependent [17]. Among the various turbulence models tested, the low Reynolds number k-ω Shear Stress Transport (SST) model is believed by some researchers [15, 18-20] to show better results than other Reynolds-Averaged Navier-Stokes (RANS) models in simulating supercritical flows given the wall region is well resolved ($y^+ \sim 1.0$). In addition, high-fidelity methods like Direct Numerical Simulation (DNS) have also been used to produce detailed information to enhance understanding of heat transfer deterioration and to assist the improvement of turbulence models [6, 21-24]. However, such methods are currently still restricted to relatively low Reynolds numbers and simple geometries due to the huge computational cost.

With the accumulation of knowledge derived from these studies, researchers began to study heat transfer in 'real' SCWR fuel channels to assist engineering development. One of the simplest ways is to make use of the data obtained previously

on simple geometries, e.g., in the case of a circular tube. Correlations have been

developed assuming that the heat transfer behavior in a SCWR sub-channel is similar to

a corresponding tube of equal hydraulic diameter. However, this is not reliable in many

cases, e.g., the HTD in tubes may not occur in a SCWR bundle with spacer grids at similar

flow and thermal conditions [25]. Therefore, experimental or numerical studies can

provide more useful information if they are based on a representative configuration

that closely resembles the whole reactor bundle. The most intensively studied

configuration in open literature is the single SCWR sub-channel due to its low computing

cost [26-29]. In order to capture the complex exchanges among sub-channels, studies

have also been widely carried out on configurations including multiple sub-channels,

such as 2×2 square bundle and 7-rod hexagon bundle [17, 30]. The results obtained

indicated that both the geometry and orientation of the rod bundle can have a

significant effect on the flow and thermal behavior in a SCWR.

This study is part of the blind benchmarking excise organized by an IAEA CRP on

SCWR aimed at improving the understanding of the thermal-hydraulic phenomena

relevant to SCWRs and assessing the predictive capability of the numerical tools and

methods. The benchmarking data was produced in an experimental facility with a 2×2

rod bundle operated at conditions resembling those of an 'industrial' SCWR. Details of

the experiment are given in Section 2. The most interesting parameter in this

benchmarking exercise is the cladding temperature that was measured using embedded

thermocouples mounted at various axial and circumferential locations in the

experimental rig. Experimental data to date are available only for two sub-critical cases,

but not yet available for the supercritical cases studied. In this paper, simulations were

carried out using two different CFD packages, one is an open-source CFD code

Code_Saturne developed by EDF R & D [31], and the other one is the commercial code

ANSYS Fluent [32]. Both packages are unstructured-grid based finite volume CFD codes.

Spatial mesh, turbulence model and discretization schemes used in these two software

packages were kept the same when possible so that the sensitivity of the results to

numerical tools could be assessed.

2. DESCRIPTION OF EXPERIMENT

2.1 Test Facility

The benchmarking experiment was conducted in the University of Wisconsin-

Madison (UW) high-pressure heat transfer test facility located in Stoughton, Wisconsin,

US [33]. It consists of a primary flow loop where the coolant is pumped into a heated

test section and a secondary flow loop used for heat removal. Figure 1 is a schematic of

the primary flow loop. The maximum operating pressure and temperature of the system

are 25 MPa and 400℃, respectively. The test section is a vertical square duct enclosing

a 2×2 rod bundle, providing a maximum of 400 kW of heat to the fluid. The rod bundle is

aligned by spacer grid which has a similar shape as that of the adjacent square channel

in the portion exposed to the working fluid, allowing them to minimize the reduction of

the flow area which is about 17% of the total flow area. Therefore, they do not cause

significant disturbances to the flow.

Journal of Nuclear Engineering and Radiation Science

Six spacer grids are welded in between five duct segments to create the full length of the test section which is 2151.5 mm. It is slightly longer than the heated length which is 2000 mm. Figure 2 shows one of the five sections. Two spacer grids are located outside the range of the heated section. The first one is before the start of the heated section and the second one is after the end of the heated section. Figure 3 shows the dimensions of the cross-section of the test section and corresponding spacer grids. The total flow area is 3.9 cm^2 and the pitch-to-diameter ratio is 1.33.

An axial cosine power profile is provided by the heater in the experiment to simulate the power distribution during fission reactions within nuclear fuel rods. The power profile is given by the equation followed,

$$q = q_{av}\left\{\theta_0 + \theta_1 \cos\left[2\theta_2\left(\frac{z}{L} - 0.5\right)\right]\right\} \qquad (1)$$

where q is the local heating power, q_{av} is the mean heating power per rod, z is the axial height from the start of heated section, L is the total length of the heated section ($L = 2$ m), θ_0, θ_1 and θ_2 are constants given by

$\theta_0 = 0.8187$

$\theta_1 = 0.6813$

$\theta_2 = 2.436$.

Ten embedded thermocouples are mounted at various axial and circumferential locations on each heated rod to measure the solid surface temperature, whilst eight bulk thermocouples are used to monitor the bulk fluid temperature at six different axial

6

Journal of Nuclear Engineering and Radiation Science

locations. The last axial location is monitored by three bulk thermocouples each 90°

apart. Details can be found in Figure 4 and Table 1.

2.2 Studied Cases

Four cases are studied in this work. They can be divided into two groups in terms

of operating pressure. Group I includes two 'subcritical' cases, i.e. Case-A and Case-B, in

which the operating pressure is around 8 MPa, far below the critical pressure of water

(22.1 MPa). The incompressibility of liquids at 'normal' conditions means that the

buoyancy force caused by density variation is thought to play an insignificant role in

comparison to the pressure and viscous forces. Therefore, it is to be expected that

numerical predictions of wall temperatures in such cases will compare closely with the

experimental data, as the current CFD tools are relatively mature in handling single-

phase forced convection problems. In contrast, the operating pressure is 25 MPa in the

Group II cases (Case-C and Case-D), so they are 'super critical' cases. The q'/G ratios

(heat flux/mass flux) used in Group II cases are much higher than those used in Group I

cases in order to ensure that the pseudo-critical temperature (384.9°C) can be reached

at certain heights of the heated channel. As such, the complex physics related to drastic

physical property changes of a fluid crossing through the pseudo-critical point (shown in

Figure 5) could cause potential difficulties in numerical simulations. This may also lead

to unexpected deviations when comparing the predictions of different numerical tools

due to the high sensitivity of the flow to details of modelling tool and mesh setups. An

overview of the cases studied in this work can be found in Table 2. It should be noted

that higher heating power is imposed in Case-C, though, the anticipated temperature

7

increase is lower than that of Case-D due to a lower q'/G ratio. Thus, the stronger

buoyancy effect would be expected to occur in Case-D.

3. METHODOLOGY

3.1 Turbulence model

Considering the fact that the low Reynolds number k-ω SST model has been

found to have excellent performance in predicting supercritical flows among various

RANS models in a number of studies [15, 18, 20], it is used to account for turbulence

throughout this study. However, it is also reported that the performance of the RANS

turbulence models may also depends on the implementation in specific CFD codes [34].

To ensure a fair comparison of the simulations results produced by ANSYS Fluent and

Code_Saturne, the relevant parameters/constants of the k-ω SST model are set the

same in the two codes.

3.2 Geometry and Mesh

The symmetric nature of the rod bundle means that it is not necessary to

simulate the full geometry. The smallest possible representative section (i.e. 1/8 of the

channel) was selected to build up the model and has been highlighted using red lines in

Figure 6(a). Figures 6(b) and 6(c) show a cross-sectional view normal to the stream-wise

direction of the extruded mesh at regions with and without a spacer grid, respectively.

To capture the complex physics in the boundary layer of buoyancy influenced flows, a

very fine near-wall grid is used for major solid boundaries (i.e. the outer surfaces of the

heated rods and the inner surface of the square duct) to resolve the viscous sub-layer,

leading to totally 10.3 million mesh cells. The y^+ value is then maintained around 1.0 for

8

these boundaries. It should be pointed out that the mesh resolution for some of the

spacer surfaces are relatively low. This is a compromise to ensure the consistency and

conformality of the mesh. Such a localized loss in mesh resolution is not expected to

affect the overall picture of the results, as the spread of the numerical error incurred is

suppressed by diffusion within a short distance from its originated place.

3.3 Solving Enthalpy

In Code_Saturne, either temperature or enthalpy is available as the field variable

for the energy equation. For the subcritical condition cases studied in this work, it

doesn't matter to use temperature or enthalpy as they are associated linearly with each

other, which can be seen in Figure 7(a). However, the situation is very different for

supercritical conditions in which temperature is insensitive to the energy change in the

vicinity of the pseudo-critical point due to the extremely high values of the specific heat

(see Figure 7(b)). As a consequence, solving temperature may potentially lead to

inaccurate results compared with solving enthalpy at a similar computing cost.

Therefore, enthalpy form of the energy equation is solved throughout this study. To

achieve a high simulation efficiency, a high resolution enthalpy-based physical property

table is then generated using NIST data base REFPROP 9.0 and implemented in

Code_Saturne (v5.3) for physical property update during the simulations. The property

table in Code_Saturne is based on a uniformly distributed enthalpy at an interval of 500

J/kg, corresponding to a smallest temperature interval of 0.005℃. Linear interpolation

is used to account for missing physical properties, which ensures a high accuracy of the

physical property calculation. In Fluent, the enthalpy is the default variable for such kind

of flows and the NIST database can be enabled directly as it has been embedded in the

version used (v16.1). Different from Code_Saturne, the physical property update in

Fluent is a little bit more computational expensive as they are calculated at each time

step using the correlations provided by the database rather than a pre-generated

property look-up table.

3.4 Numerical Strategy

A pressure-based transient fractional-step solver is used in both codes for time

advancement. Second order upwind schemes are employed for spatial discretization of

the momentum and the energy equation. A fully developed flow profile is imposed at

the inlet of the domain and a buffer section is added after the last spacer grid to

minimize the impact of the outlet boundary condition on the main flow region, see

Figure 8. All walls are assumed to be non-slip smooth walls. The y^+ value of the first cell

for the main walls, e.g. except for the spacer region, is kept around 1.0, especially for

Group II cases. Simulations were run on a Tier 2 cluster located at Science and

Technology Facilities Council Daresbury Laboratory in the UK. The simulation were

typically run using 16 CPU nodes providing totally 512 cores. Convergence was ensured

in both codes by monitoring the major flow variables at various locations in the flow

domain. A statistically steady state was finally reached after a sufficient physical time

being simulated.

4. RESULTS AND DISCUSSION

Simulations were first run with the mesh described in Section 3.1 using both

Code_Saturne and Fluent. Figures 9(a) and 9(b) are comparisons of the axial

Journal of Nuclear Engineering and Radiation Science

temperature distribution between simulation results and experimental data for the two

subcritical cases of Group I. The bulk temperature and circumferential averaged wall

temperature are sampled along the stream-wise direction every 5 mm from the start to

the end of the heated section. They are calculated using the following equations,

$$T_{bulk,z_0} = \int_{z=z_0} \rho \vec{u} T \cdot d\vec{A} \bigg/ \int_{z=z_0} \rho \vec{u} \cdot d\vec{A} \tag{2}$$

$$T_{wall,z_0} = \int_{z=z_0} T dA_s \bigg/ \int_{z=z_0} dA_s \tag{3}$$

Where T is the local temperature, °C, $\vec{u}$ is the local velocity vector, m/s, $\vec{A}$ is the face

vector of the cross section of the entire flow channel, m², A_s is the area of the rod

surface of a cell height at the axial location z_0, m/s.

It can be seen that the evolution of bulk temperatures predicted by the two

codes both agree very well with the experimental data in Group I cases. They almost

overlap each other. However, the predicted averaged wall temperatures deviate from

each other by a maximum of 2°C in Case-A and 5°C in Case-B. The Fluent results seem

to compare slightly better with experiments than those of Code_Saturne; the latter lie

closer to the upper bound of the experimental data range, especially for Case-B,

suggesting that the wall temperature is potentially over estimated. This may be due to

the relatively high sensitivity of Code_Saturne to the near wall mesh since less

numerical treatments are usually used to reduce such sensitivity in an open source code

compared against commercial codes, which was evidenced through a previous mesh

sensitivity test for Code_Saturne and Fluent conducted using an unheated pipe flow

(Results can be found in Figure 10 in which Code_Saturne shows a higher response of

11

the fractional factor to the y^+ value of the wall adjacent cells. The frictional factor used

here refers to the Darcy frictional factor, defined as $f = 8\tau_w / \rho U^2$). To possibly increase

the simulation accuracy, a finer mesh with 60.9 million cells was generated, i.e., Mesh-2

shown in Figure 11(b). The y^+ value reduces accordingly below 0.5 for all the major walls.

However, the wall temperatures derived using the new mesh shift slightly towards the

Fluent results by no more than 1℃ in both of the Group I cases, suggesting that the

relatively high mesh sensitivity of Code_Saturne has no significant effects in simulations

of subcritical forced convection problems. Hence, the results, including those derived

using the coarser mesh (Mesh-1), can be regarded as mesh independent. The different

predictions in wall temperature of the two codes could be attributed to the potential

different ways of implementation of the k-ω SST turbulence model.

It is also worth noticing that the spacer grids have small but noticeable impacts

on the overall distribution of the wall temperature when the fluid passes through the

spacer region. The wall temperature reduces suddenly due to the disruption of the

thermal boundary layer by the spacer grid and the relatively higher turbulence

intensities induced in the spacer region. Troughs can be observed at axial locations of

0.3 m, 0.8 m, 1.2 m and 1.6 m, corresponding to the spacer grids in the heated section

(spacer grid II to V).

Compared with the two sub-critical cases in Group I, the results of the

supercritical cases in Group II show drastic difference in axial distribution of wall

temperature which increases sharply when approaching the pseudo-critical point,

leading to a huge difference from the bulk, see Figures 9(c) and 9(d). The huge increase

12

Journal of Nuclear Engineering and Radiation Science

in wall temperature can be attributed to flow laminarization happening in the boundary layer, which impairs the heat transfer therein. Additionally, it should be noted that the laminarized boundary layer is delicate and can be reversed locally by disturbances induced from the spacer grids, leading to wall temperature spikes (i.e. sharp decrease followed by sharp increase) in the wake just downstream of the spacer grids.

In Case-C, both Code_Saturne and Fluent well capture the onset and termination of HTD, but the latter predicts a much lower level of HTD, resulting in a significant deviation in wall temperature prediction from the former. The onset of HTD happens at the axial location where the wall temperature approaches the pseudo-critical point, which is approximately about 0.34 m downstream of the start of the heated section. The HTD tends to decay significantly after the fourth spacer grid which is located about 1.2 m away from the start of the heated section. In Case-D, on the other hand, the two codes only agree with each other on the onset of HTD (about 0.2 m downstream of the start of the heated section) which, though tends to die out earlier in the Fluent prediction (about 1.2 m downstream of the start of the heated section) than that of Code_Saturne (more than 1.5 m downstream of the start of the heated section). It should be noted that significant difference in wall temperature predictions happens in both Case-C and Case-D when using Code_Saturne on the two meshes, especially in the regions where HTD happens, suggesting that the low mesh sensitivity observed in the aforementioned forced convection cases is dramatically amplified in buoyancy-aided mixed convection flows. In Case-C, the finer mesh result in the prediction of the wall

13

temperature to be closer to that of Fluent, however, the trend is completely reversed in Case-D.

In order to see more clearly the occurrence and development of the flow laminarization in Group II cases, the axial velocity and the turbulent shear stress are further plotted along the radial direction at cross sections of different axial positions. It should be noted here that the turbulent shear stress is calculated based on the Boussinesq hypothesis of isotropic turbulence, in which the relevant stress component is calculated as the corresponding component of the strain rate multiplied with the eddy viscosity derived through the turbulence model. As can be seen in Figure 12(a), for Case-C, the velocity profile starts to flatten around z=0.5 m due to the near-wall fluid acceleration caused by the buoyancy force and fully flattens at some point between z=0.5 m and z=0.9 m (note the velocity profile is slightly M-shaped at z=0.9 m), followed by significant M-shaped profiles (e.g. at z=1.1 m), and then recovers to normal shapes again (e.g. z=1.5 m and z=1.8 m). Accordingly, the turbulent shear stress experiences firstly a decrease and then an increase (see Figure 12(b)), indicating the occurrence of flow laminarization and recovery. However, it should be pointed out that the recovery happens here is not likely to be caused by a stronger buoyancy effect as that normally happens in the cases with uniform-heating. Instead, it is more likely due to the weakened buoyancy effect in the higher section of the channel where heating power is diminishing, which brings the velocity profile back towards its normal shape. Figures 12(c) and 12(d) are results for Case-D accordingly. In general, the overall picture is similar to that of Case-C, but the suggested buoyancy effect is more significant.

14

Journal of Nuclear Engineering and Radiation Science

Figure 13(a) shows the axial distribution of the static pressure of the four cases. It is to be expected that a linear pressure drop with constant form losses at spacer grids is observed in Case-A and Case-B, since they are purely forced convections. In such cases, the flow is expected to be fully developed between the spacers, thus resulting in a uniform frictional loss. This is no longer the case in Case-C and Case-D in which buoyancy plays an important role and turbulence varies significantly along the flow. In Case-D, the buoyancy effect is so strong that a negative pressure drop even occurs in the higher section of the channel. Flow acceleration is another notable feature in strong heating flows. Figure 13(b) shows the bulk velocity along the axial direction. It can be seen clearly that no significant flow acceleration occurs in the Group I cases since the thermal expansion is negligible. In contrast, the flow accelerates to about twice the magnitude of the initial velocity in both cases of Group II. The flow acceleration is a direct response to the thermal expansion of the fluid, which happens more significantly when the increasing bulk temperature passes through the pseudo-critical point where the fluid becomes gas-like.

Flow laminarization resulting from a distorted velocity profile due to buoyancy is believed to be the reason for the HTD. This is further evaluated using the heat transfer coefficient (HTC) and buoyancy parameter $\mathbf{Bo}^*$ which can be calculated as follows,

$$\mathbf{Bo}^* = \frac{\mathbf{Gr}^*}{\mathbf{Re}^{3.425}\mathbf{Pr}^{0.8}} \qquad (4)$$

where $\mathbf{Re}$ and $\mathbf{Pr}$ are the Reynolds number and Prandtl number, respectively. The $\mathbf{Gr}^*$ is the Grashof number based on the wall heat flux, which is calculated as

15

$$\mathbf{Gr}^* = \frac{g\beta q' D_h^{\,4}}{\lambda v^2} \tag{5}$$

where g is acceleration of gravity, m/s^2, β is the thermal expansion factor, 1/K, q' is the

wall heat flux, W/m^2, D_h is the hydraulic diameter, m, λ is the thermal conductivity,

W/m·K, v is the kinematic viscosity, m^2/s.

The two parameters are plotted along the axial direction for both Group I and

Group II cases and can be found in Figures 13(c) and 13(d), respectively. In general, the

HTC spikes appear around the locations where the spacer grids are installed. This can be

attributed to the disruption of the thermal boundary layer and locally enhanced heat

transfer related to structure-induced turbulence. For the Group I cases, an overall

decrease of within 10% in HTC can be observed throughout the whole test section,

indicating that the heat transfer is not impaired significantly. In contrast, a sharp

decrease of about 80% happens in both Group II cases, suggesting the occurrence of

HTD. Correspondingly, Figure 13(d) shows the evolution of the buoyancy parameter

along the axial direction for all of the cases studied. It can be seen that only Case-D

meets the criterion of $\mathbf{Bo}^* > 5.7\times10^{-7}$ in which case the buoyancy effect is significant. It

should be pointed out here that the criterion was established based on normal fluid at

atmosphere pressure. In practice, a lower value is suggested to be used in evaluating

the buoyancy effect in supercritical pressure fluids [35]. In addition the recovery of HTC

in Group II cases that occurs in the second half of the test section is not due to the

increase of the buoyancy effect (which is expected to be decreasing in these regions

according to the distribution of the buoyancy parameter), instead, it is merely due to

the reduced heating on the rods.

16

Journal of Nuclear Engineering and Radiation Science

5. CONCLUSIONS

This work contributes to assessing the widely used k-ω SST turbulence model (implemented in two of the major CFD tools, namely, Fluent and Code_Saturne) in capturing the underlying physics in buoyancy-aided flows of water at supercritical conditions, which is essential in the design and development of SCWRs. A numerical model is built-up based on a benchmarking experiment carried out in a 2×2 rod bundle operated with water at subcritical and supercritical pressures. The model is firstly validated for subcritical conditions, as the relevant experimental data had already been released to the benchmarking participants. The experimental data are still not available for supercritical cases. Despite this, numerical results are presented in this paper for both supercritical cases. The numerical simulations predict the occurrence of flow laminarization and HTD within the boundary layer in both of the mixed convection cases. Such predictions will be re-assessed in detail once the experimental data are available.

The secondary aim of this work is to evaluate the performance of the open-source CFD tool Code_Saturne in simulating supercritical flows. Through the simulations, the code is found to be stable and robust with the k-ω SST turbulence model, even though some localized low mesh resolutions are used on non-important walls as a compromise to ensure mesh conformality. For the sake of comparison, the well-known commercial code ANSYS Fluent was also used to generate simulation results with the same model setups. Overall, both codes agree with each other in predicting some major physics in mixed convections like flow laminarization and HTD. However, Code_Saturne

17

tends to be more responsive to buoyancy effects and thus gives higher wall temperature

predictions. Understanding the reason behind is part of the future work.

ACKNOWLEDGMENT

NOMENCLATURE

A	Area, m^2
$\vec{A}$	Face vector of the cross section of the rod bundle, m^2
C_p	Specific heat, J/kg·K
D_h	Hydraulic diameter, m
f	Darcy frictional factor
g	Acceleration of gravity, m/s^2
G	Mass flux at the inlet of the rod bundle, $kg/m^2 \cdot s$
k	Turbulent kinetic energy, J/kg

18

L	Total length of the heated section, m
P	Operating pressure, MPa
q	Heating power, kW/rod
q'	Wall heat flux, W/m²
T	Temperature, K
$\vec{u}$	Velocity vector, m/s
u'	x-direction velocity fluctuation, m/s
U	Bulk velocity, m/s
v'	y-direction velocity fluctuation, m/s
y^+	Dimensionless wall distance
z	Axial height from the start of the heated section of the rod bundle, m

Greek Letters

β	Thermal expansion factor, 1/K
λ	Thermal conductivity, W/m·K
μ	Molecular viscosity, Pa·s
ν	Kinematic viscosity, m²/s
ρ	Density, kg/m³
τ_w	Wall shear stress, Pa
ω	Specific dispassion rate, 1/s

Non-Dimensional Numbers

Bo* — Buoyancy parameter; $\left(\dfrac{\mathbf{Gr}^*}{\mathbf{Re}^{3.425}\mathbf{Pr}^{0.8}} \right)$

Gr* — Grashof number; $\left(\dfrac{g\beta q' D_h^{\ 4}}{k\nu^2} \right)$

Pr — Prandtl number; $\left(\dfrac{\mu C_p}{k} \right)$

Re — Reynolds number; $\left(\dfrac{\rho U D_h}{\mu} \right)$

Subscripts and Superscripts

av — Averaged value

bulk — Bulk properties

in — Inlet of the rod bundle

s — Rod surface properties

wall — Wall properties

Acronyms and Abbreviations

ANSYS — Analysis System

BEIS — Business, Energy and Industry Strategies

CFD — Computational Fluid Dynamics

CPU — Central Processing Unit

20

CRP	Coordinated Research Projects
DNS	Direct Numerical Simulation
EDF	Électricité de France
Exp.	Experiment
Fluent	Name of a commercial CFD software
HTC	Heat Transfer Coefficient
HTD	Heat Transfer Deterioration
IAEA	International Atomic Energy Agency (Vienna, Austria)
NIST	National Institute of Standards and Technology (USA)
R & D	Research & Development
RANS	Reynolds Averaged Navier-Stokes
REFPROP	Reference Fluid Thermodynamic and Transport Properties
SCWR	Super Critical Water-cooled Reactor
SST	Shear Stress Transport
TC	Thermal Couple
UK	United kingdom
UW	University of Wisconsin-Madison

Journal of Nuclear Engineering and Radiation Science

REFERENCES

[1] Heusener, G., Muller, U., Schulenberg, T., and Squarer, D., 2000, "A European Development Program for a High Performance Light Water Reactor (HPLWR)," *Proc. 1st International Symposium on Supercritical Water Cooled Reactor Design and Technology*, Tokyo, Japan, November 6-9, pp. 23-28.

[2] Oka, Y., and Koshizuka, S., 2001, "Supercritical-Pressure, Once-through Cycle Light Water Cooled Reactor Concept," Journal of Nuclear Science and Technology, **38**(12), pp. 1081-1089. DOI: 10.1080/18811248.2001.9715139

[3] Jackson, J. D., and Hall, W. B., 1979, "Forced Convection Heat Transfer to Fluids at Supercritical Pressure," Chapter in Turbulent Forced Convection in Channels and Rod Bundles, Editors: S. Kakac and D. B. Spalding, Hemisphere, Washington, USA, vol. 2, pp. 563 611.

[4] Jackson, J. D., and Hall, W. B., 1979, "Influences of Buoyancy on Heat Transfer to Fluids Flowing in Vertical Tubes under Turbulent Conditions," Chapter in Turbulent Forced Convection in Channels and Rod Bundles, Editors: S. Kakac and D. B. Spalding, Hemisphere, Washington, USA, vol. 2, pp. 613 640.

[5] Abdulmohsin, R. S., and Al-Dahhan, M. H., 2016, "Axial Dispersion and Mixing Phenomena of the Gas Phase in a Packed Pebble-Bed Reactor," Annals of Nuclear Energy, **88**, pp. 100-111. DOI: 10.1016/j.anucene.2015.10.038

[6] Bae, J. H., Yoo, J. Y., and Choi, H., 2005, "Direct Numerical Simulation of Turbulent Supercritical Flows with Heat Transfer," Physics of Fluids, **17**(10), pp. 105104. DOI: 10.1063/1.2047588

[7] He, S., Jiang, P. X., Shi, R., Kim, W. S., and Jackson, J. D., 2004, "Computational Study of Convective Heat Transfer to CO2 at Supercritical Pressure in a Vertical Mini Tube," *Proc. 2nd International Conference on Microchannels and Minichannels*, Rochester, New York, USA, June 17-19, Paper #2348, 8 pages.

[8] He, S., Jiang, P.-X., Xu, Y.-J., Shi, R.-F., Kim, W. S., and Jackson, J. D., 2005, "A Computational Study of Convection Heat Transfer to CO2 at Supercritical Pressures in a Vertical Mini Tube," International Journal of Thermal Sciences, **44**(6), pp. 521-530. DOI: 10.1016/j.ijthermalsci.2004.11.003

[9] S. He, W. S. Kim and J. H. Bae, 2008, "Assessment of Performance of Turbulence Models in Predicting Supercritical Pressure Heat Transfer in a Vertical Tube," International Journal of Heat and Mass Transfer, **51**(19-20), pp. 4659-4675. DOI: 10.1016/j.ijheatmasstransfer.2007.12.028

22

[10] He, S., Kim, W. S., Jiang, P. X., and Jackson, J. D., 2004, "Simulation of Mixed Convection Heat Transfer to Carbon Dioxide at Supercritical Pressure," Proceedings of the Institution of Mechanical Engineers Part C: Journal of Mechanical Engineering Science, **218**(11), pp. 1281-1296. DOI: 10.1177/095440620421801101

[11] Jaromin, M., and Anglart, H., 2013, "A Numerical Study of Heat Transfer to Supercritical Water Flowing Upward in Vertical Tubes under Normal and Deteriorated Conditions," Nuclear Engineering and Design, **264**, pp. 61-70. DOI: 10.1016/j.nucengdes.2012.10.028.

[12] Liu, L., Xiao, Z., Yan, X., Zeng, X., and Huang, Y., 2013, "Heat Transfer Deterioration to Supercritical Water in Circular Tube and Annular Channel," Nuclear Engineering and Design, **255**, pp. 97-104. DOI: 10.1016/j.nucengdes.2012.09.025

[13] Kao, M.-T., Lee, M., Ferng, Y.-M., and Chieng, C.-C., 2010,"Heat Transfer Deterioration in a Supercritical Water Channel," Nuclear Engineering and Design, **240**(10), pp. 3321-3328. DOI: 10.1016/j.nucengdes.2010.06.028

[14] Sharabi, M., Ambrosini, W., He, S., and Jackson, J. D., 2008, "Prediction of Turbulent Convective Heat Transfer to a Fluid at Supercritical Pressure in Square and Triangular Channels," Annals of Nuclear Energy, **35**(6), pp. 993–1005. DOI: 10.1016/j.anucene.2007.11.006.

[15] Liu, L., Xiao, Z., Yan, X., Zeng, X., and Huang, Y., 2013, "Numerical Simulation of Heat Transfer Deterioration Phenomenon to Supercritical Water in Annular Channel," Annals of Nuclear Energy, **53**, pp.170-181. DOI: 10.1016/j.anucene.2012.08.022

[16] Ma, D., Zhou, T., and Li, B., 2017, "Diametrical Effects of Supercritical Water Heat Transfer in Annular Channels," *Proc. 17th International Topical Meeting on Nuclear Reactor Thermalhydraulics*, Xi'an, China, September 3-8, Paper #20613, 10 pages.

[17] Podila, K., and Rao, Y., 2016, "CFD Modelling of Supercritical Water Flow and Heat Transfer in a 2×2 Fuel Rod Bundle," Nuclear Engineering and Design, **301**, pp. 279-289. DOI: 10.1016/j.nucengdes.2016.03.019

[18] Palko, D., and Anglart, H., 2008, "Theoretical and Numerical Study of Heat Transfer Deterioration in High Performance Light Water Reactor," Science and Technology of Nuclear Installations, **2008**, pp. 1-5. DOI: 10.1155/2008/405072

[19] Schulenberg, T., and Visser, D. C., 2013,"Thermal-Hydraulics and Safety Concepts of Supercritical Water Cooled Reactors", Nuclear Engineering and Design, **264**, pp. 231-237. DOI: 10.1016/j.nucengdes.2012.08.040

Journal of Nuclear Engineering and Radiation Science

[20] Zhu, Y., 2010, "Numerical Investigation of the Flow and Heat Transfer within the Core Cooling Channel of a Supercritical Water Reactor," Ph.D. thesis, Institute of Nuclear Technology and Energy Systems (IKE), University of Stuttgart, Stuttgart.

[21] Nemati, H., Patel, A., Boersma, B. J., and Pecnik, R., 2015, "Mean Statistics of a Heated Turbulent Pipe Flow at Supercritical Pressure," International Journal of Heat and Mass Transfer, **83**, pp. 741-752. DOI: 10.1016/j.ijheatmasstransfer.2014.12.039

[22] Nemati, H., Patel, A., Boersma, B. J., and Pecnik, R., 2016, "The Effect of Thermal Boundary Conditions on Forced Convection Heat Transfer to Fluids at Supercritical Pressure," Journal of Fluid Mechanics, **800**, pp. 531-556. DOI: 10.1017/jfm.2016.411

[23] Wang, W., and He, S., 2015, "Direct Numerical Simulation of Fluid Flow at Supercritical Pressure in a Vertical Channel," *Proc. 16th International Topical Meeting on Nuclear Reactor Thermal Hydraulics*, Chicago, USA, August 30-September 4, pp. 2334-2347.

[24] Bae, J. H., Yoo, J. Y., Choi, H., and McEligot, D. M., 2006, "Effects of Large Density Variation on Strongly Heated Internal Air Flows," Physics of Fluids, **18**(7) pp.075102. DOI: 10.1063/1.2216988

[25] Leung, L., and Rao, Y., 2015, "A Strategy in Developing Heat-transfer Correlation for Fuel Assembly of the Canadian Super-critical Water-cooled Reactor," *Proc. 7th International Symposium on Supercritical Water-Cooled Reactors*, Helsinki, Finland, March 15-18, Paper #2031, 11 pages.

[26] Ampomah-Amoako, E., Akaho, E. H. K., Nyarko, B. J. B., and Ambrosini, W., 2013, "Analysis of Flow Stability in Nuclear Reactor Subchannels with Water at Supercritical Pressures," Annals of Nuclear Energy, **60**, pp. 396-405. DOI: 10.1016/j.anucene.2013.05.031.

[27] Gu, H. Y., Cheng X., and Yang, Y. H., 2010, "CFD Analysis of Thermal-Hydraulic Behavior of Supercritical Water in Sub-Channels," Nuclear Engineering and Design, **240**(2), pp.364-374. DOI: 10.1016/j.nucengdes.2008.08.022

[28] Podila, K., and Rao, Y. F., 2015, "CFD Analysis of Flow and Heat Transfer in Canadian Supercritical Water Reactor Bundle," Annals of Nuclear Energy, **75**, pp. 1-10. DOI: 10.1016/j.anucene.2014.07.039

[29] Rahman, M. M., Dongxu, J., Beni, M. S., Hei, H. C., He, W., and Zhao, J., 2016, "Supercritical Water Heat Transfer for Nuclear Reactor Applications: A Review," Annals of Nuclear Energy, **97**, pp. 53-65. DOI: 10.1016/j.anucene.2016.06.022

[30] Rohde, M., Peeters, J. W. R., Pucciarelli, A., Kiss, A., Rao, Y. F., Onder, E. N., Muehlbauer, P., Batta, A., Hartig, M., Chatoorgoon, V., Thiele, R., Chang, D. Tavoularis, S., Novog, D., McClure, D., Gradecka M., and Takase, K., 2016, "A Blind, Numerical Benchmark Study on Supercritical Water Heat Transfer Experiments in a 7-Rod Bundle," Journal of Nuclear Engineering and Radiation Science, **2**(2), pp.021012. DOI: 10.1115/1.4031949

[31] Fournier, Y., Bonelle, J., Moulinec, C., Shang, Z., Sunderland, A.G., and Uribe, J.C., 2011, "Optimizing Code_Saturne Computations on Petascale Systems," Computers & Fluids, **45**(1), pp. 103-108. DOI: 10.1016/j.compfluid.2011.01.028

[32] ANSYS, Inc., 2015, "ANSYS FLUENT User's Guide," Release 16.2.

[33] Kate, L., Anderson, M., 2016, "CFD Benchmark Analysis for 2x2 Fuel Rod Bundle", (private and unpublished).

[34] Xiong, J., Cheng, X., 2014, "Turbulence modelling for supercritical pressure heat transfer in upward tube flow," Nuclear Engineering & Design, 270, pp. 249-258. DOI: 10.1016/j.nucengdes.2014.01.014

[35] He, S., Kim, W. S., and Jackson, J. D., 2008,"A Computational Study of Convective Heat Transfer to Carbon Dioxide at a Pressure Just above the Critical Value", Applied Thermal Engineering, **28**(13), pp. 1662-1675. DOI: 10.1016/j.applthermaleng.2007.11.001

25

Figure Captions List

the rod bundle.

Fig. 12   Local velocity and turbulent shear stress ($-\rho<u'v'>$) profiles for Group II

cases. (Plots are based on Code_Saturne results using Mesh-2).
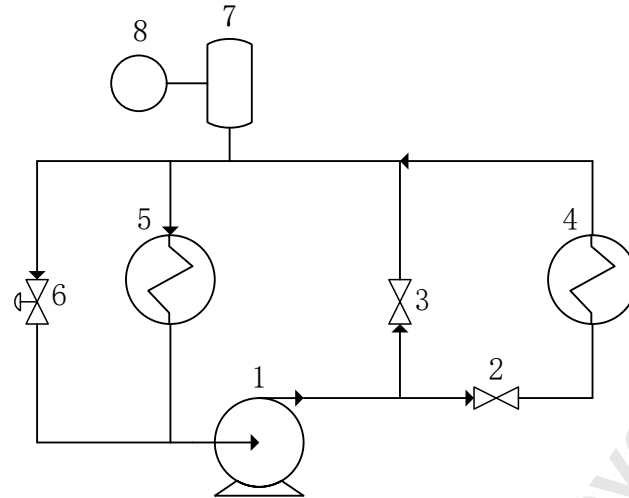
Fig. 13   Comparisons of the Case A-D on (a) axial pressure drop, (b) bulk velocity,

(c) heat transfer coefficient and (d) buoyancy parameter. (Plots are based

on Code_Saturne results using Mesh-2).

27

Table Caption List

1. High pressure pump 2. Orifice flow meter 3. Bypass orifice 4. Heated test section
5. Heat exchange 6. Bypass valve 7. Pressurizer/Accumulator 8. Argon gas cylinder

Fig. 1   Schematic of the primary flow loop in the test facility.

29
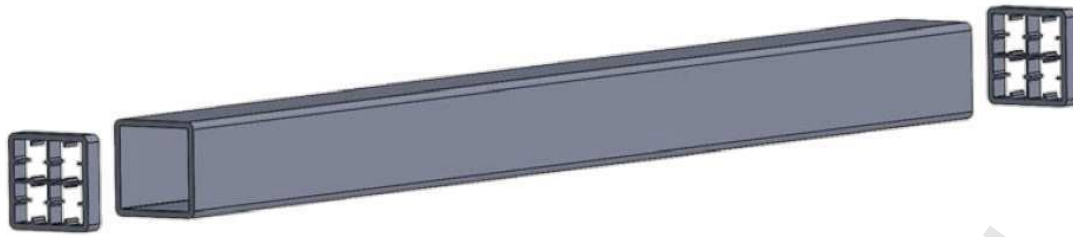
Fig. 2   Sketch of one of the five duct segments in the test section.

30
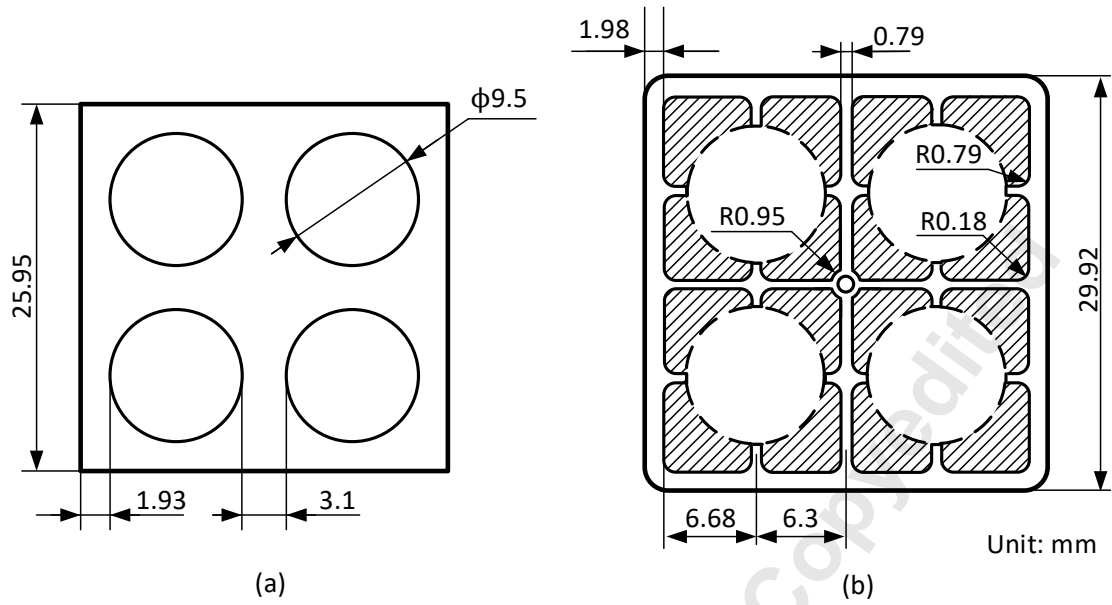
Fig. 3 Dimensions of (a) the flow channel of the test section and (b) the spacer grids
(The shading area represents the potion exposed to the working fluid).

31
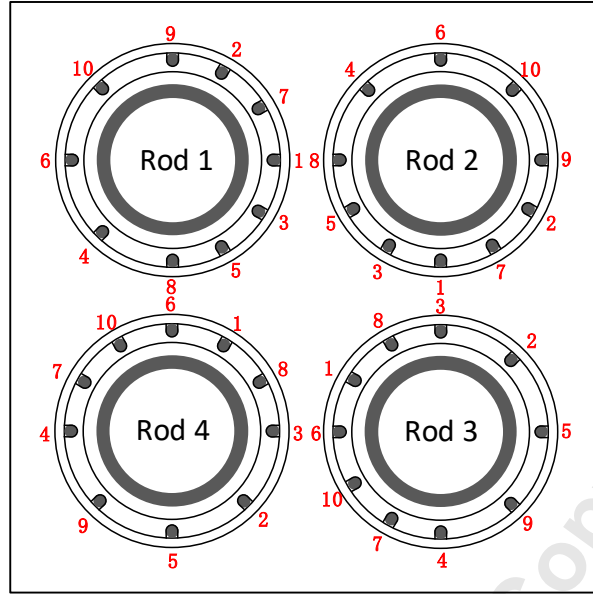
Fig. 4   Circumferential locations of the embedded thermocouples

Journal of Nuclear Engineering and Radiation Science
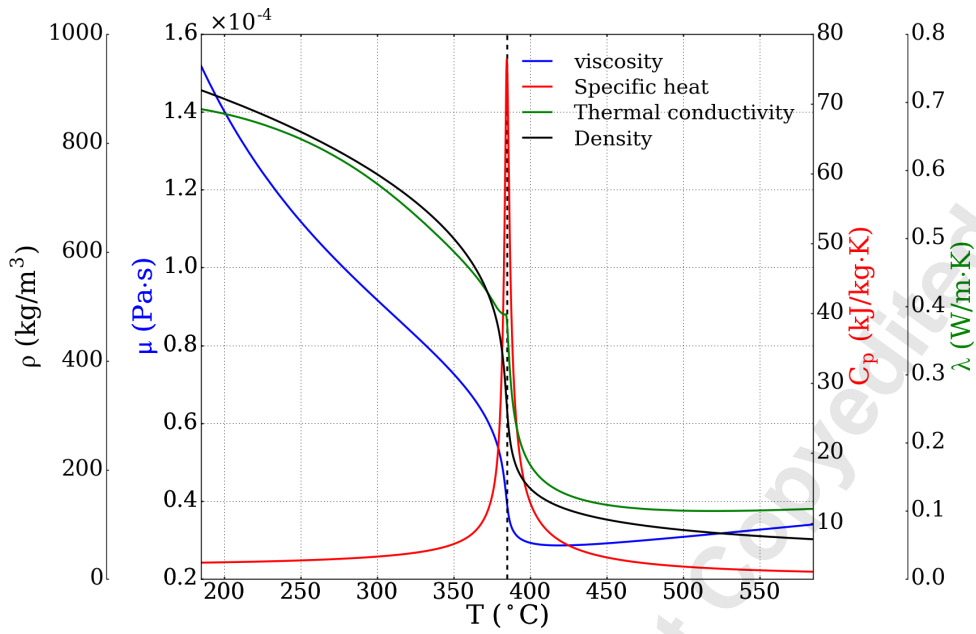
Fig. 5   Physical properties of water in the vicinity of the pseudo-critical point at 25 MPa.

33

(a)   (b)   (c)
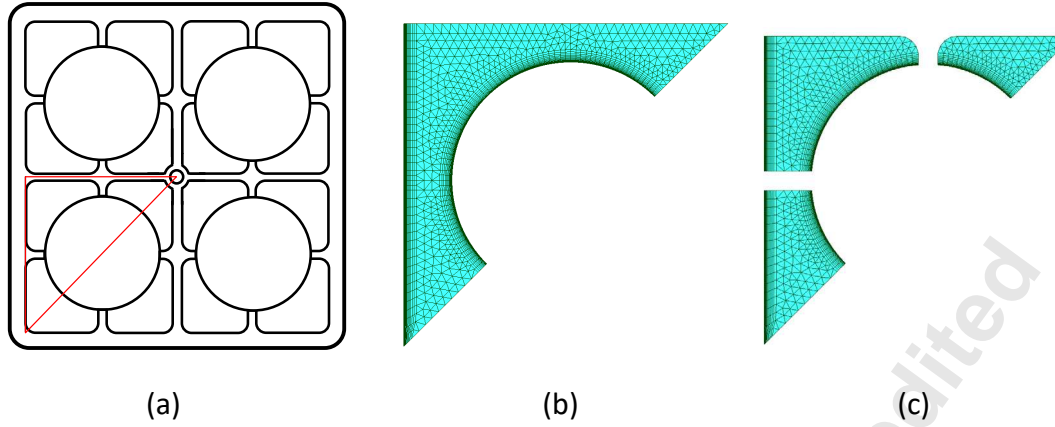
Fig. 6   Sketch of the geometry and mesh. (a) 1/8-representative section (highlighted by red lines), (b) cross-section view of the mesh for regions without spacer grid, (c) cross-section view of the mesh for regions with spacer grid.

Journal of Nuclear Engineering and Radiation Science

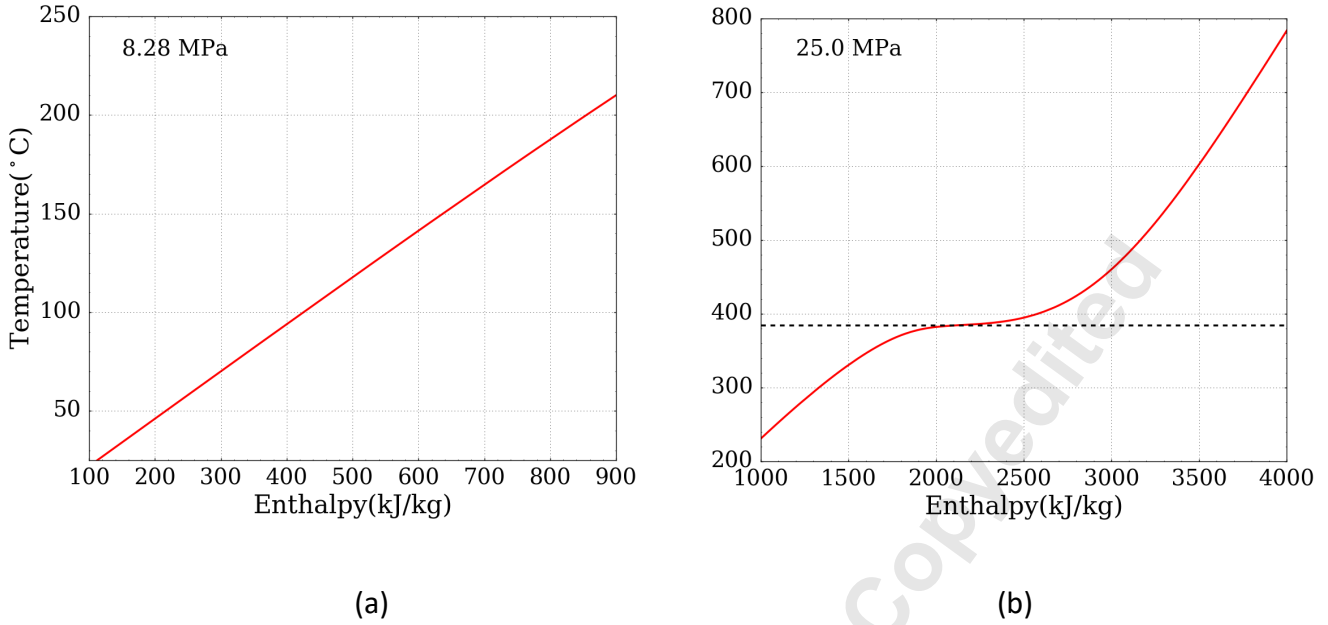(a)   (b)

Fig. 7   Variation of temperature with enthalpy for water at (a) subcritical pressure of

8.28 MPa and (b) supercritical pressure of 25 MPa.

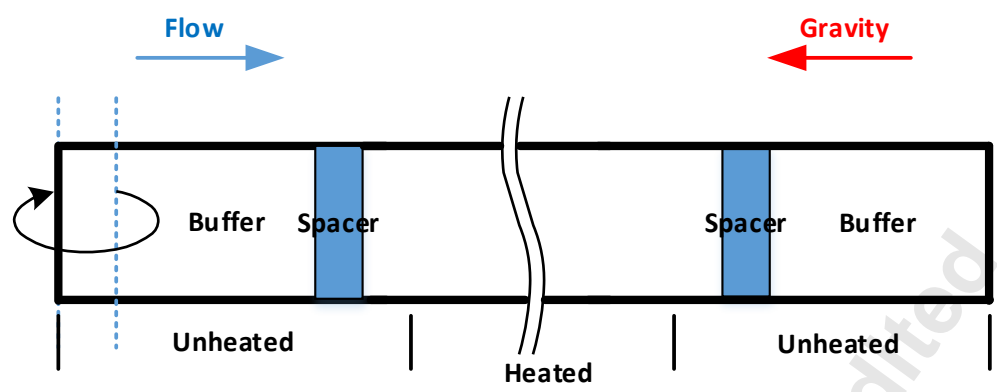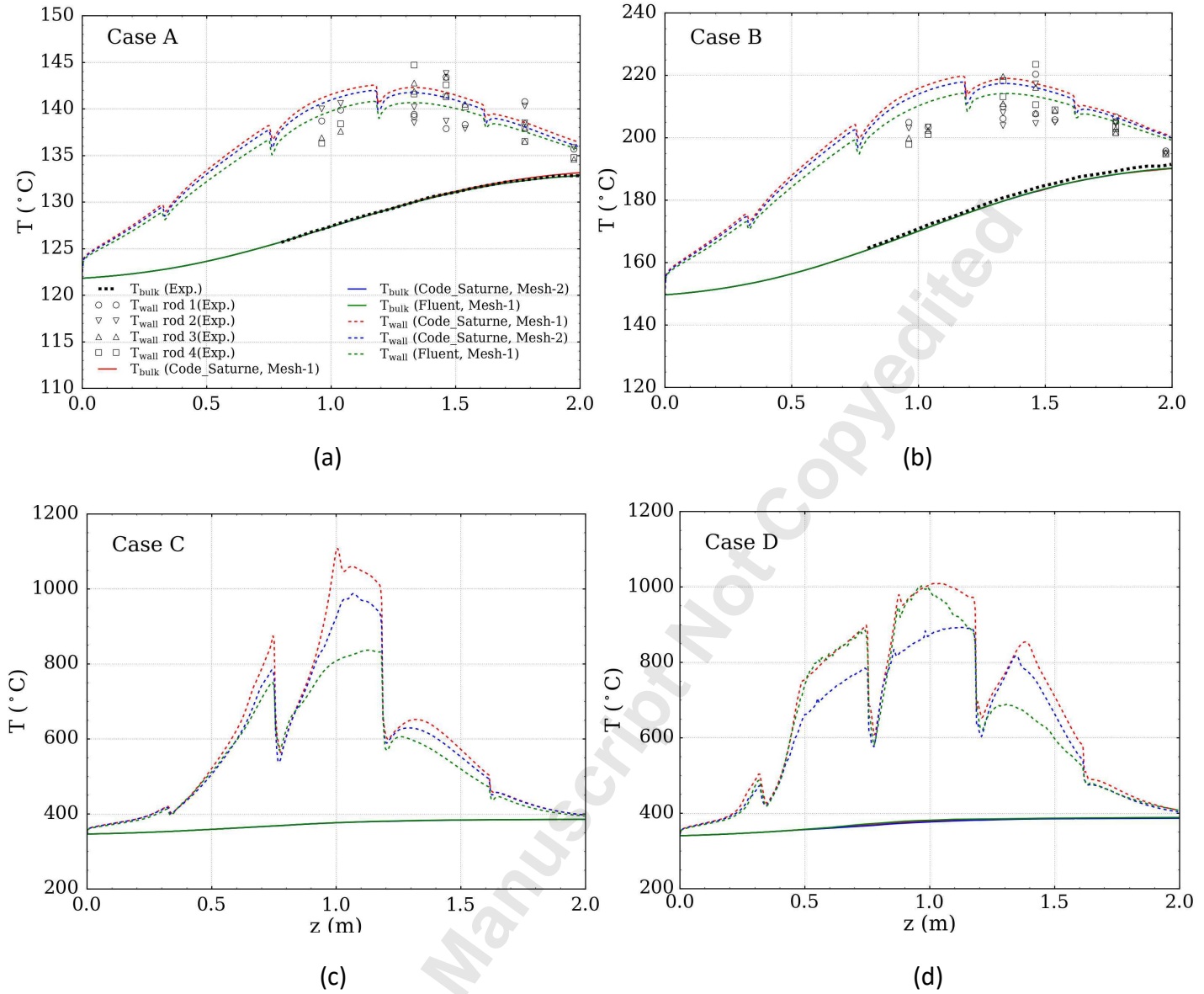Fig. 8   Schematic of the numerical model.

Fig. 9   Axial distribution of bulk temperature and circumferential averaged wall

temperature of the fuel rod.
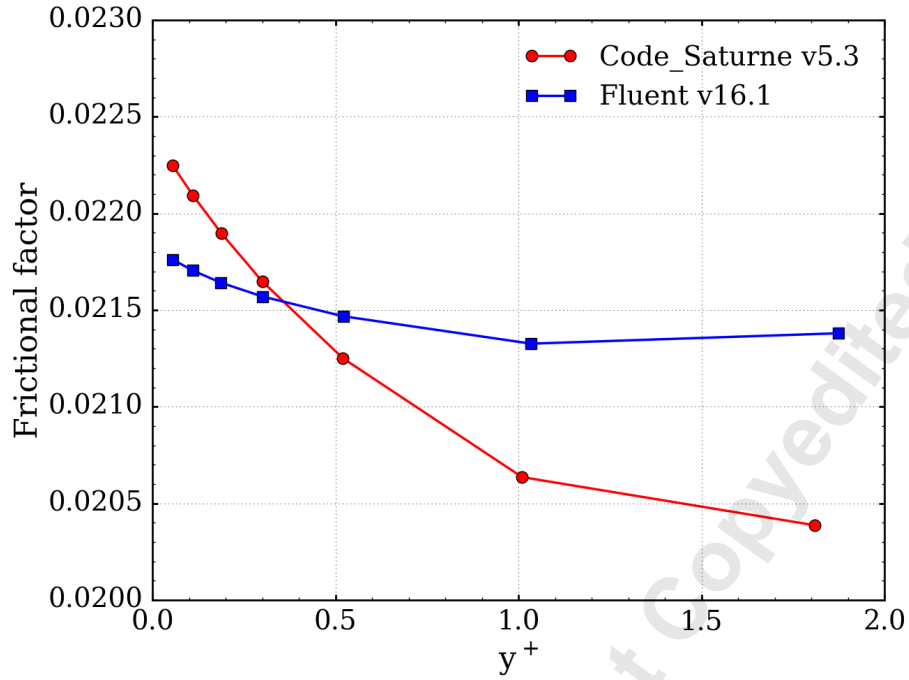
Fig. 10   A near-wall mesh sensitivity test for the k-ω SST turbulence model implemented
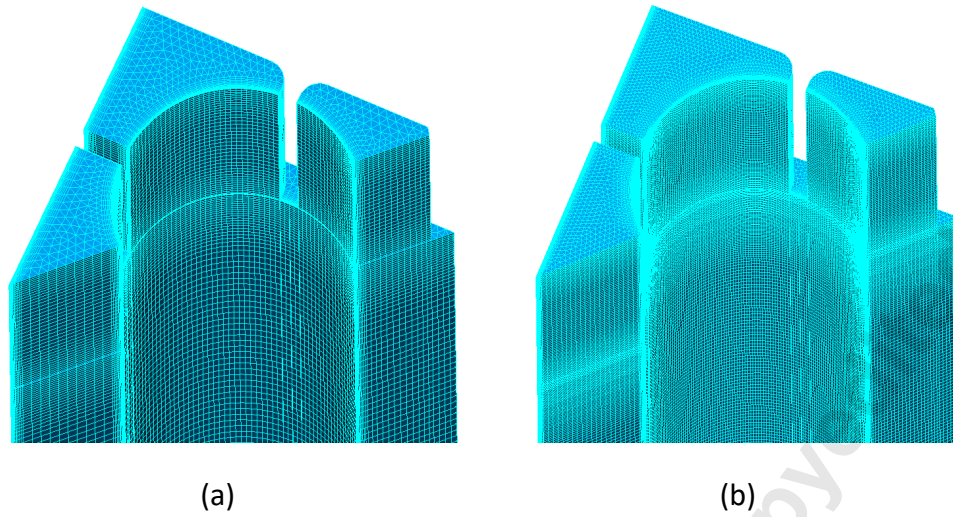
in Code_Saturne and Fluent.

(a)   (b)

Fig. 11   Section views of (a) Mesh-1 and (b) Mesh-2 at one of the spacer grids in the rod

bundle.

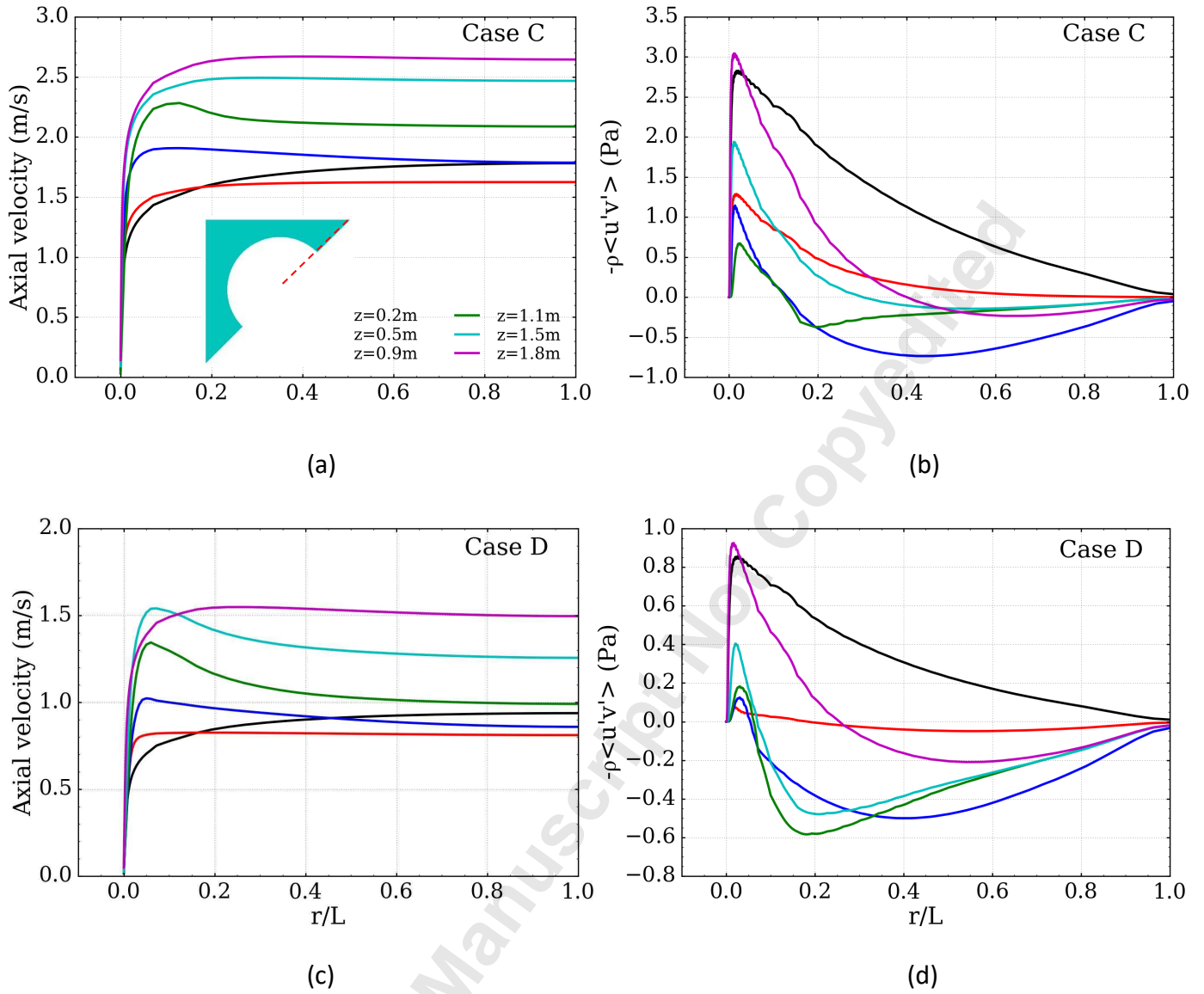Fig. 12   Local velocity and turbulent shear stress ($-\rho<u'v'>$) profiles for Group II cases.

(Plots are based on Code_Saturne results using Mesh-2).

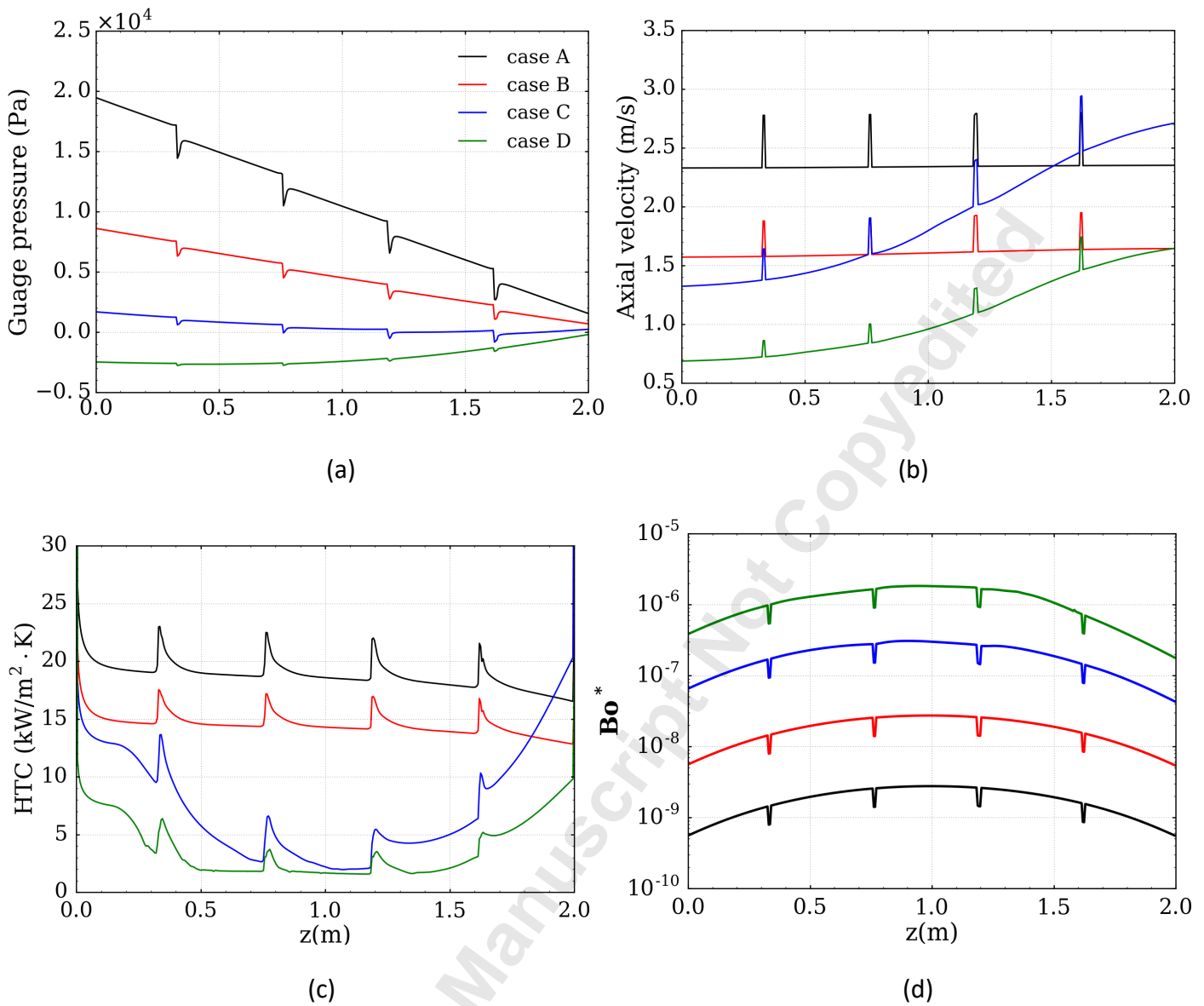Journal of Nuclear Engineering and Radiation Science

Fig. 13   Comparisons of the Case A-D on (a) axial pressure drop, (b) bulk velocity, (c)

heat transfer coefficient and (d) buoyancy parameter. (Plots are based on Code_Saturne

results using Mesh-2).

41

Journal of Nuclear Engineering and Radiation Science

Table 1 Overview of the cases studied.

Group	Case	P_{in} (MPa)	T_{in} (°C)	G (kg/m^2·s)	q_{av} (kW/rod)
I	A	8.26	121.8	2201	10.07
	B	8.28	149.6	1447	24.96
II	C	25.0	346.0	844	47.8
	D	25.0	340.0	450	32.9

Journal of Nuclear Engineering and Radiation Science

Table 2 Locations of the embedded and bulk thermocouples

	Rod Internal Thermocouples			Bulk Thermocouples	
TC No.	Angular location (°)		Axial location (mm from start of the heated section)	Bulk TC No.	Axial location (mm from start of the heated section)
	Rods 1/2	Rods 3/4	Rods 1/2/3/4		
1	0	330	961.9	1	579
2	60	225	1038.1	2	1038
3	330	270	1333.5	3	1333
4	225	90	1333.5	4	1462
5	300	180	1462.0	5	1538
6	180	0	1462.0	6/7/8	1778
7	60	60	1538.2		
8	270	300	1778.0		
9	90	135	1778.0		
10	135	30	1974.6		